Facet-Dependent Disorder in Pristine High-Voltage Lithium–Manganese-Rich Cathode Material

Hemant Dixit,*,†,§ Wu Zhou,†,§ Juan-Carlos Idrobo,‡ Jagjit Nanda,*,†,⊥ and Valentino R. Cooper*,†

†Materials Science and Technology Division and ‡Center for Nanophase Materials Sciences, Oak Ridge National Lab, Oak Ridge, Tennessee 37831, United States and ⊥Department of Chemical and Biomolecular Engineering, University of Tennessee, Knoxville, Tennessee 37996. §H.D. and W.Z. contributed equally to this work.

ABSTRACT Defects and surface reconstructions are thought to be crucial for the long-term stability of high-voltage lithium–manganese-rich cathodes. Unfortunately, many of these defects arise only after electrochemical cycling which occurs under harsh conditions, making it difficult to fully comprehend the role they play in degrading material performance. Recently, it has been observed that defects are present even in the pristine material. This study, therefore, focuses on examining the nature of the disorder observed in pristine $Li_{1.2}Ni_{0.175}Mn_{0.525}Co_{0.1}O_2$ (LNMCO) particles. Using atomic-resolution *Z*-contrast imaging and electron energy loss spectroscopy measurements, we show that there is indeed a significant amount of antisite defects present in this material, with transition metals substituting on Li metal sites. Furthermore, we find a strong segregation tendency of these types of defects toward open facets (surfaces perpendicular to the layered arrangement of atoms) rather than closed facets (surfaces parallel to the layered arrangement of atoms). First-principles calculations identify antisite defect pairs of Ni swapping with Li ions as the predominant defect in the material. Furthermore, energetically favorable swapping of Ni on the Mn sites was observed to lead to Mn depletion at open facets. Relatively, low Ni migration barriers also support the notion that Ni is the predominant cause of disorder. These insights suggest that certain facets of the LNMCO particles may be more useful for inhibiting surface reconstruction and improving the stability of these materials through careful consideration of the exposed surface.

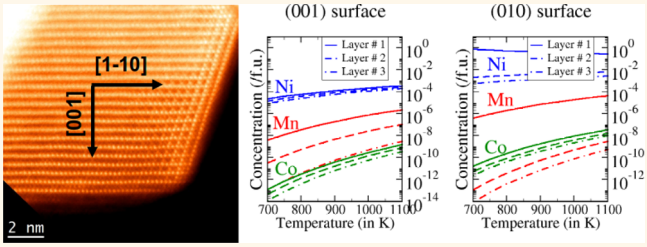

KEYWORDS: Li-ion battery · antisite defects · Ni segregation · surface · migration barriers

Current lithium-ion battery technology is limited by the availability of high-energy density cathodes. During the past decade, there have been significant efforts toward the development of high-voltage (>5 V) cathode materials. Notable among these are lithium–manganese-rich layered oxides and high voltage spinels.[1−4] In particular, lithium–manganese-rich cathodes have almost two times greater capacities compared to conventional cathodes, such as the widely used commercial $LiCoO_2$ when cycled above 4.5 V.[5] These lithium-rich $Li(Li_yNi_{x-y}Mn_xCo_{1-2x})O_2$ oxides, more aptly written as $xLi_2MnO_3\cdot(1-x)LiMO_2$ (M = Mn, Ni, Co), are solid solutions with ordered nanosized domains limited to a few layers along the *c*-axis.[6]

Unfortunately, these high-voltage cathode compositions have structural and chemical instabilities, which emerge during electrochemical cycling, thereby limiting their use in heavy-duty applications such as plug-in hybrid electrical vehicles. The structural and phase instabilities are manifested in terms of a progressive decay or loss of charge and a discharge voltage plateau during cycling (known as voltage fade). It has been shown that the reduction of the voltage plateau is accompanied by the migration or diffusion of transition metal (TM) cations in the host lattice.[7−11] For instance, the high-voltage layered oxide undergoes a number of irreversible surface and interfacial processes during its first electrochemical charge cycle, such as the loss of oxygen[12] and reactions of the highly charged cathode surface with the electrolyte.[13] Literature reports suggest that the phase transformation, from a layered to a spinel-like phase, is initiated by intersite exchange between the Li and TM cations and the concomitant segregation of the Mn-rich phase.[6,14−17] Recently, we and others[14] have observed

* Address correspondence to dixithm@ornl.gov, nandaj@ornl.gov, coopervr@ornl.gov.

Received for review October 8, 2014 and accepted November 21, 2014.

Published online November 21, 2014
10.1021/nn505740v

intersite exchange behavior even in the pristine material. As such, a mechanistic understanding of the surface reconstructions and the formation of antisite defects in this pristine material may enable novel design approaches where disorder can be pursued as a strategy for retaining high-energy densities.[18]

In this article, using a synergistic combination of atomic scale experimental and theoretical techniques, we investigate the origin of the TM disorder observed in the pristine (uncycled) $Li_{1.2}Ni_{0.175}Mn_{0.525}Co_{0.1}O_2$ (LNMCO) cathode material. Atomic-resolution *Z*-contrast imaging and electron energy loss spectroscopy (EELS) experiments, performed in an aberration-corrected scanning transmission electron microscope (STEM), show the presence of antisite defects in the bulk and predominantly at the surface. Interestingly, the EELS scan along the [1$\bar{1}$0] direction shows higher concentrations of Ni antisite defects compared to the [001] direction. The surfaces along these two directions are oriented differently with respect to the layered arrangements of the Li, oxygen, and TM atoms in the LNMCO cathode material. First-principles calculations indicate that the experimentally observed TM antisite defects are prevalently Ni antisites, both in the bulk and at the surface. Furthermore, the defect formation energies are facet-dependent with "open" surfaces (*i.e.*, surfaces exposing the alternating Li, oxygen, and TM layers to the vacuum along the [1$\bar{1}$0] direction) having higher concentrations of antisite defects as compared to "closed" surfaces (parallel to the layered arrangement of Li, oxygen, and TM layers along the [001] direction). EELS measurements also show significant depletion of Mn at the surface for open facets. First-principles calculations reveal that this is due to the preferential substitution of Ni at the Mn site. Additionally, Ni atoms have the lowest migration energy barriers for inter- and intralayer diffusion among the group of TM atoms, which indicate higher mobility of Ni in the LNMCO cathode material. These findings suggest that surface segregation can be minimized by shape-control synthesis of LNMCO particles, where the primary cathode particle has preferred crystallographically oriented facets, thus providing a path for controlling the stability and performance of these materials.

RESULTS AND DISCUSSION

Figure 1 shows an atomic-resolution *Z*-contrast image of bulk LNMCO, where alternating lithium–oxygen–transition metal layers can be observed. A relatively large concentration of antisite defects (TM replacing Li) in the Li layers (brighter spots in the dark-contrast rows in the figure) can also be seen. However, with this image alone, one cannot distinguish which TM atom among Ni, Mn, or Co forms the antisite defect. Moreover, EELS experiments to quantify the relative concentration of the TM antisite defects at each Li column require spectra with a high signal-to-noise ratio, which is not possible due to electron-beam damage to the sample. As such, we performed first-principles calculations to investigate the nature and formation energies of TM antisite defects present in the Li layers. It is important to note that the mobility of the Li^+ ions in and out of the layered structure determines battery performance.[19] Here, the presence of TM atoms in the Li layer results in the formation of nanoscale inhomogeneities, which may significantly affect Li-ion mobility.

Two types of antisite defects (M_{Li}) are considered—nonstoichiometric substitutional antisite defects (a Li atom is replaced with a TM atom from reservoir) and stoichiometric antisite defect pairs (*i.e.*, Li and TM atoms are interchanged between their respective layers). The bulk LNMCO cathode material was modeled by constructing a $2\sqrt{3} \times 2\sqrt{3}$ supercell from the

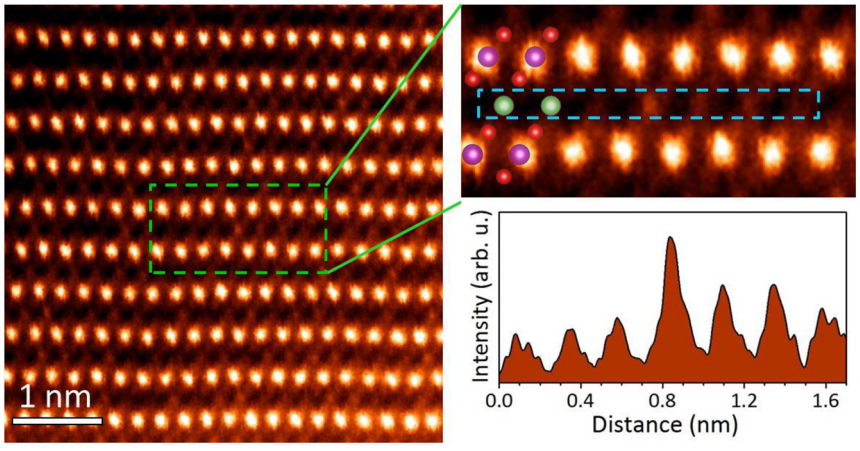

Figure 1. Experimental *Z*-contrast STEM image taken along the [110] zone axis, showing the presence of antisite defects in the bulk layered structure. The brighter atomic rows correspond to TM planes, while the darker atomic rows are Li planes. (Right) Enlarged *Z*-contrast image and the corresponding image intensity line profile acquired from the region highlighted by the dashed cyan rectangle. Some Li atomic columns display much higher image intensity than their neighboring Li sites (see the overlaid structure model: Li, green; TM, magenta; O, red), arising from the presence of TM antisites in these Li columns.

TABLE 1. Formation Energy (in eV) of Transition Metal, M (M = Ni, Mn, and Co), Substitutional, and Antisite Pair Defects in the LNMCO Cathode Material

type		Ni	Mn	Co
bulk				
M_{Li} substitutional		3.94	3.24	3.80
M_{Li} antisite pair		0.52	1.76	1.71
(010) surface	layer no.			
M_{Li} substitutional	1	3.37	3.07	3.35
M_{Li} antisite pair	1	−0.18	1.42	1.26
M_{Li} antisite pair	2	0.18	1.68	1.33
M_{Li} antisite pair	3	0.26	1.84	1.38
(001) surface	layer no.			
M_{Li} substitutional	1	3.09	2.15	2.80
M_{Li} antisite pair	1	0.45	1.15	1.56
M_{Li} antisite pair	2	0.48	1.34	1.62
M_{Li} antisite pair	3	0.51	1.68	1.70

parent $LiMnO_2$ hexagonal crystal. Each layer (either Li or TM or oxygen) in the model supercell contains 12 atoms, which were arranged in *ABC* stacking, resulting in a total of 144 atoms. Earlier theoretical calculations proposed a broken zigzag arrangement of the Ni atoms in the TM layer for the $Li[Li_{1/6}Ni_{1/4}Mn_{7/12}]O_2$ cathode material.[20] Using this model as a starting point, we further incorporated Co atoms by replacing one of the Ni atoms in the transition metal layer, leading to $Li[Li_{2/12}Ni_{2/12}Mn_{7/12}Co_{1/12}]O_2$ stoichiometry. In this configuration, the Co atoms prefer a site that bridges adjacent Ni atoms within their broken zigzag arrangement. The optimized lattice parameters of the supercell were $a = b = 9.80$ Å and $c = 14.87$ Å, in reasonable agreement with the experimental values of $a = b = 9.63$ Å and $c = 14.80$ Å reported for similar compositions.[6]

The calculated formation energies of the substitutional antisite defects in bulk LNMCO are 3.94, 3.24, and 3.80 eV for Ni, Mn, and Co, respectively (Table 1). On the other hand, the formation energies of the antisite defect pairs are drastically lower than the substitutional antisite defects: 0.52, 1.76, and 1.70 eV for Ni, Mn, and Co, respectively. The relatively high formation energies of substitutional antisite defects result in extremely low concentration ($\sim 10^{-19}$/fu using eq 2 in the Methods section), ruling out their presence in the LNMCO cathode material. In other words, stoichiometric disorder is favored compared to the nonstoichiometric disorder in bulk LNMCO. Among the TM atoms, Ni has the lowest formation energy whereas the formation energies of Mn and Co are comparable to each other.

Although EELS experiments of individual antisites were not possible, we were able to acquire EELS line scans near the surface of the LNMCO particles along the $[1\bar{1}0]$ and [001] directions intersecting the exposed $(1\bar{1}2)$ and (001) planes, respectively (see Figure 2a,b), where defects can be easily observed in the *Z*-contrast images. Surprisingly, the acquired EEL spectra show changes in the concentrations of the TM atoms at the LNMCO surface depending on orientation. For the $[1\bar{1}0]$ direction, the EEL profile shows a strong enhancement of the Ni signal within ~1.5 nm from the surface that is associated with a notable structural reconstruction along the $(1\bar{1}2)$ plane. Simultaneously, a decrease in the intensity of the Mn signal is observed while the Co intensity remains almost unaffected. Similar segregation of Ni atoms toward the surface was also experimentally observed in $Li_{1.2}Ni_{0.2}Mn_{0.6}O_2$ particles[15,21] and also in $Li_{1.2}Mn_{0.61}Ni_{0.18}Mg_{0.01}O_2$ particles.[22] In contrast, the [001] direction shows only a slight variation in the TM composition in a narrow region (~0.5 nm) near the surface.

To elucidate the facet-dependent segregation of Ni to the surface, we calculated the formation energies of antisite pairs near the LNMCO surface. Here, we consider two surface geometries, the (010) and (001) surface. It should be noted that simulating the exact experimental geometry along the $(1\bar{1}2)$ plane as shown in Figure 2 requires large supercells, which are computationally prohibitive. Nevertheless, the $[1\bar{1}0]$ direction in the experiment is normal to the $(1\bar{1}0)$ plane, which is equivalent to the (010) surface in the hexagonal lattice. Moreover, the (010) surface closely resembles the $(1\bar{1}2)$ surface in the EELS experiment with both possessing an alternating arrangement of Li and TM columns perpendicular to the surface (open facet) and the $(1\bar{1}2)$ planes can also be viewed as a collection of $(1\bar{1}0)$ planes with atomic steps. The surface geometry was modeled using a ~3 nm thick slab, which was constructed by doubling the 144 atom bulk supercell along the *b*- and *c*-directions. The periodic images of the slab were separated by ~12 Å of vacuum to minimize their interaction. The (010) surface was terminated by a mixture of cations and anions, and the (001) surface was terminated by an oxygen layer (see Figures 3 and 4 (left panel)).

First, we discuss the (010) surface. The formation energies of the antisite pairs in the first, second, and third layers, as illustrated in Figure 3 (left panel), were calculated and are listed in Table 1. The calculated formation energies of the antisite pairs in the first layer were −0.18, 0.77, and 1.26 eV for Ni, Mn, and Co, respectively. In contrast to bulk, we observed that the formation of Ni antisite pairs in the first layer of the (010) surface is favorable, while the formation energies of Mn and Co antisite pairs are significantly reduced. Furthermore, a systematic study of the layer-by-layer formation energies reveals an increase in the formation energies, approaching the bulk limit, as we move away from the surface. Thus, a larger concentration of defects is expected in the surface region than in the bulk, indicative of a tendency toward surface segregation of the TM antisites as observed in the EELS experiment.

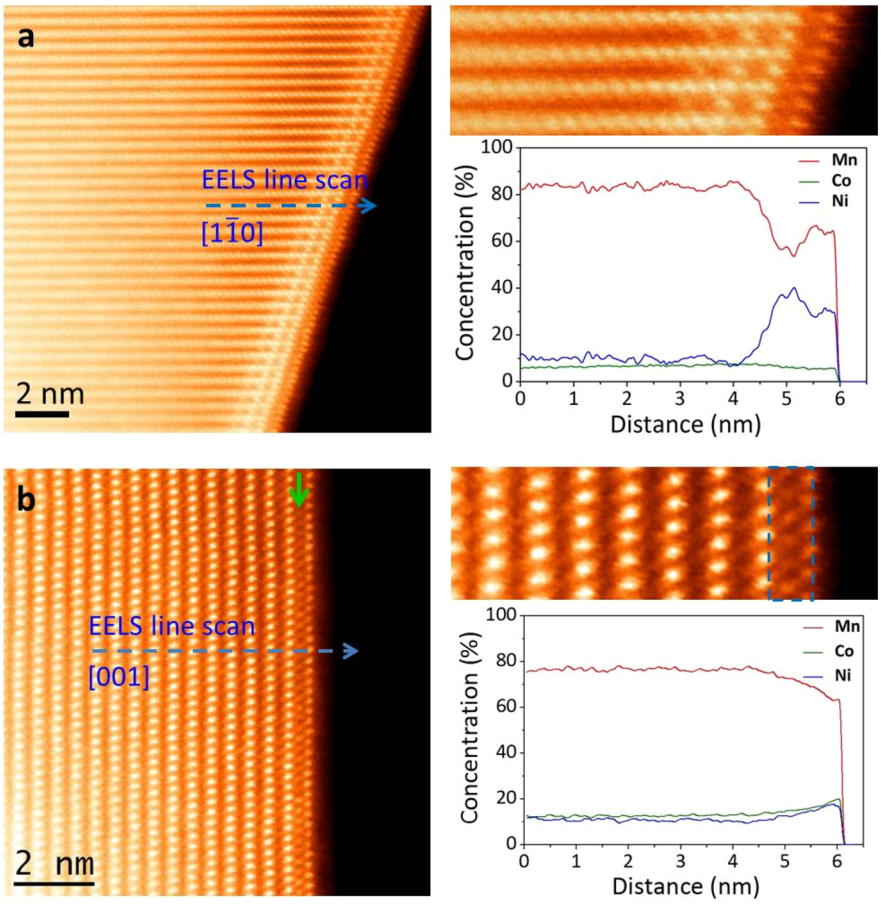

Figure 2. *Z*-contrast images and EELS line scan profiles for a LNMCO particle along the (a) [1$\bar{1}$0] and (b) [001] direction. The panels on the right show the close-ups of the surface regions and the relative concentration line profiles obtained from EELS. Surface reconstruction and segregation of Ni in the reconstructed layers are observed along the (1$\bar{1}$2) plane. For the (001) plane, however, there is a slight increase in antisite defect concentration in the first Li layer, as highlighted by the green arrow. The Ni and Co concentrations also increase slightly in the surface region, but no significant segregation or reconstruction was observed in contrast to the (1$\bar{1}$2) plane.

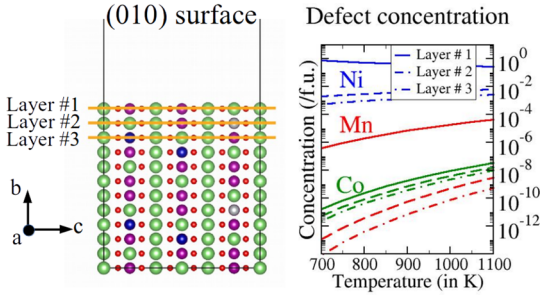

Figure 3. Schematic for (010) surface geometry of LNMCO (Li, green; TM, magenta; O, red) and the corresponding equilibrium defect concentrations at high temperatures. Antisite pairs are formed by replacing Li with a TM atom in the vertical Li columns.

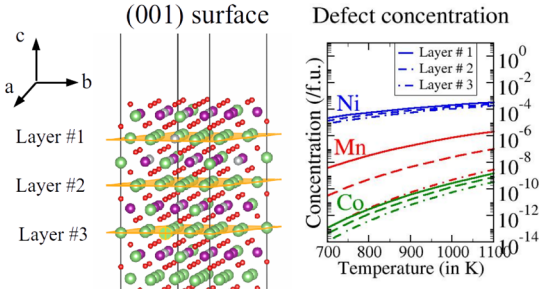

Figure 4. Schematic for (001) surface geometry of LNMCO (Li, green; TM, magenta; O, red) and the corresponding equilibrium defect concentrations at high temperatures. Antisite pairs are formed by replacing Li with a TM atom in the Li layers.

We also observed that the TM−oxygen bonds in the open facet are elongated by ∼1−2%, resulting in Jahn−Teller distorted MO_6 (M = TM atom) octahedra.

Next, we considered the (001) slab which contained six layers of Li and TM atoms and 12 layers of oxygen. The calculated formation energies of the antisite pairs in the first layer are 0.45, 1.15, and 1.56 eV for Ni, Mn, and Co, respectively. The formation energies at the surface are lowered compared to their bulk counterpart by 0.07, 0.56, and 0.24 eV for Ni, Mn, and Co, respectively. Jahn−Teller distorted MO_6 (M = TM atom) octahedra were also observed for the closed facets; however, these are minimized compared to the open facets.

The lowering of the formation energies at the surface was also observed in the case of substitutional antisite defects. As listed in Table 1, we find that the formation energies of the substitutional antisite defects at either the (010) or (001) surfaces were reduced relative to their bulk counterpart. However, they were still significantly higher than those of the antisite pair defects, indicating that the antisite pairs are predominant.

To analyze the prevalence of each antisite pair defect species, we have calculated the defect concentrations using the formation energies obtained from our first-principles calculations. A solid-state synthesis approach is typically used to prepare the LNMCO cathode material, and it involves high temperatures in the range of 700−1100 K. Defects are usually formed during synthesis at high temperature and may be retained in the sample owing to their slow diffusion at lower temperatures. At thermodynamic equilibrium, the defect concentration is proportional to the formation energy and it can be computed using the Boltzmann distribution function (eq 2 in the Methods section). The calculated defect concentrations for the TM antisite pairs as a function of temperature are shown in Figures 3 and 4 (right panel). The calculations clearly indicate that Ni antisite pairs are the dominant defects, having significantly larger concentrations than Mn or Co antisite pairs. Thus, the Ni antisite pairs are the leading cause of disorder in the LNMCO cathode material, both at the surface and in the bulk.

Another interesting feature observed in the EELS was the depletion of Mn at the $(1\bar{1}2)$ surface. Since the overall stoichiometry of the LNMCO cathode material is unchanged, one possibility is the substitution of Mn with Ni atoms from adjacent TM layers. The calculated formation energies for the Ni_{Mn} antisite pairs are −0.40 and 0.35 eV for the (010) and (001) surfaces, respectively. The results indicate that the formation energies are facet-dependent, and Ni−Mn swapping is only favored at the (010) surface, as seen in the EELS profile. The (001) surface, on the other hand, should show less dramatic changes in the TM concentration near the surface, again observed in the EELS profile.

Finally, we evaluated the migration barriers for TM atoms moving into adjacent Li vacancy sites in the bulk to examine their diffusion kinetics. The migration barriers were calculated along two different paths: (1) within the TM layer along the [010] direction of the supercell (intralayer diffusion) and (2) between the TM and Li layer along the [111] direction of the supercell (interlayer diffusion). The energy barriers for both the in-plane and out-of-plane diffusion are shown in Figure 5. Among the group, the Ni atoms have the lowest energy barriers for intra- and interlayer diffusion. Furthermore, the energy barrier for Ni diffusion is about 1 eV, which is comparable to that of the Li ion.[15] The similar mobilities of Li and Ni atoms are due to their

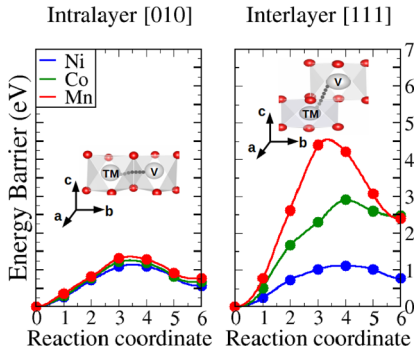

Figure 5. Energy barrier for intralayer [010] and interlayer [111] diffusion of the TM antisite defect to the nearest Li vacancy site.

comparable ionic radii. The Mn and Co atoms, on the other hand, require significant activation energies for out-of-plane movement (interlayer), whereas their in-plane (intralayer) diffusion barriers are marginally higher than the Ni cations. The higher mobility of Ni again contributes to the probability that Ni cations are the leading cause of disorder within these materials.

CONCLUSIONS

In conclusion, we have shown that the Ni antisite pairs are the leading cause of the disorder experimentally observed in the LNMCO cathode material. A significant concentration of Ni antisite pairs is expected during the solid-state synthesis of these layered oxides, which could be dependent on controllable experimental synthesis conditions, such as annealing temperature and the stoichiometry of the cathode composition. Moreover, the formation energies of antisite pairs are facet-dependent with open facets, that is, surfaces perpendicular to the layered arrangement of the Li, oxygen, and TM layers, showing significant Ni segregation toward the surface. Mn and Co antisite pairs are also present but in significantly lower concentrations than Ni. An interesting result is the Mn depletion and simultaneous enhancement in the Ni concentration at the $(1\bar{1}2)$ surface as observed experimentally in EELS. Our calculations on a similar (010) surface confirm that this may be due to the preferential swapping of surface Mn cations with Ni ions from adjacent layers. We also find a lower migration energy barrier for Ni atoms compared to Mn and Co, for both intra- and interlayer diffusion. More importantly, the Ni migration barrier is comparable to that of the Li ion, which implies that both Ni and Li have similar mobilities during electrochemical cycling. The prevalence of Ni antisite pair defects along with their low migration barrier for both intra- and interlayer diffusion suggests a plausible mechanism for Ni segregation. A large number of Ni antisites are formed during synthesis, and later they migrate toward the surface, segregating selectively in the first Li surface layer as confirmed by both theory and experiment. Interestingly, the formation energies and surface

reconstructions are facet-dependent with the $(1\bar{1}2)$ facet having higher concentrations of antisite pairs and reconstructions compared to the (001) facet. Hence, the selection of appropriate facets of the LNMCO particles can be used to minimize the surface segregation of the Ni atoms, which may have important implications for the cathode performance and stability.

METHODS

The LNMCO material having nominal composition, $Li_{1.2}Ni_{0.175}Mn_{0.525}Co_{0.1}O_2$, was obtained from the pilot scale facility of Toda-Kogyo Corporation, Japan. This class of cathode materials is generally synthesized using standard co-precipitation methods forming TM hydroxide or carbonate precursors followed by reacting with $LiOH \cdot H_2O$ at higher temperatures (900 °C).[23] Atomic-resolution *Z*-contrast imaging and EELS experiments were performed in an aberration-corrected STEM, Nion UltraSTEM 100, which has a cold field-emission electron source and can correct third- and fifth-order aberrations.[24] The microscope was operated at a 100 kV acceleration voltage, using a 30 mrad probe-forming semiangle, a 48 mrad EELS collection aperture angle, and an energy dispersion of 0.5 eV/channel. The experiments were performed using an electron beam of ~1 Å in diameter with ~50 pA nominal probe current. A dwell time of 0.15 s per pixel and a step size of 0.5 Å were used for the EELS line scans. STEM ADF images were taken before and after the EELS line scans to ensure that no obvious structural change was induced by the electron beam. The low accelerating voltage (100 kV) used in our experiment also helps to reduce electron beam damage, as compared to typical 200 or 300 kV settings used.[25] The EELS signals for the TM elements were integrated over 30 eV energy windows, after background subtraction, for quantification of their relative concentrations. Theoretical investigations were performed using density functional theory within the generalized gradient approximation by Perdew, Burke, and Ernzerhof and the projector-augmented plane-wave (PAW) method[26,27] as implemented in the VASP package.[28] The PAW potentials used explicitly treat 1 valence electron for Li ($2s^1$), 10 for Ni ($3d^84s^2$), 9 for Co ($3d^74s^2$), 7 for Mn ($3d^54s^2$), and 6 for oxygen ($2s^22p^4$). An energy cutoff of 520 eV was used with a Monkhorst–Pack special *k*-point grid of $2 \times 2 \times 1$. Ions were relaxed until the forces on each atomic site were below 10 meV/Å and simultaneously achieved a total energy convergence of 10^{-6} eV. To describe the effect of localized d electrons of the 3d TM ions, the Hubbard parameter $U = 5.96$, 5.00, and 3.40 eV was applied for Ni, Mn, and Co, respectively. The applied effective *U* values are consistent with earlier calculations and provide an accurate estimation of the formation enthalpy of stable binary oxides, in good agreement with the experiment.[20,29,30] The $2\sqrt{3} \times 2\sqrt{3} \times 1$ supercells consisting of 144 atoms for bulk and 288 atoms with 12 Å vacuum for the surface were used. The migration barriers were calculated using the nudged elastic band method,[31] choosing a set of five images between the initial and final state. The defect formation energy ($E_f[D^q]$) for a defect (D) in a charge state q was defined as

$$E_f[D^q] = E_{tot}[D^q] - E_{tot}[\text{bulk}] + \sum_i n_i\mu_i + q[E_F + E_v + \Delta V] \quad (1)$$

where $E_{tot}[D^q]$ is the total energy of the supercell containing the defect, $E_{tot}[\text{bulk}]$ is the total energy of the supercell without a defect, n_i is the number of atoms of the type i ($n_i > 0$ if an atom is added and $n_i < 0$ if an atom is removed), and μ_i is the corresponding chemical potential which is determined using the formation enthalpy of stable binary oxides—NiO, Mn_3O_4, and Co_3O_4. E_F is the Fermi energy with respect to the top of the valence band, E_v, of the primitive unit cell. ΔV is the difference in the reference potential of the supercell with and without a defect. In the presence of defects, the position of band edges (valence band maximum, conduction-band minimum) are affected, and the term ΔV is used for correct band alignment. Here we used a simple and computationally economical method to calculate ΔV which is discussed in ref 32. The defect concentration under thermal equilibrium can be obtained using

$$C(D_A^q) = C(A_A)\exp^{(-E_f(D_A^q)/k_BT)} \quad (2)$$

where $C(A_A)$ is the concentration of site A without any defect, k_B is the Boltzmann constant, and T is the temperature.

Conflict of Interest: The authors declare no competing financial interest.

Acknowledgment. This work was supported by the U.S. Department of Energy, Basic Energy Sciences, Materials Sciences and Engineering Division (V.R.C. and H.D.), and the Office of Science Early Career Research Program (V.R.C.). J.N. acknowledges funding support from the Assistant Secretary for Energy Efficiency and Renewable Energy, Office of Vehicle Technologies of the U.S. Department of Energy. W.Z. acknowledges the Wigner Fellowship through the Laboratory Directed Research and Development Program of Oak Ridge National Laboratory, managed by UT-Battelle, LLC, for the U.S. DOE. Part of this research supported by the Center for Nanophase Materials Sciences (CNMS), which is sponsored at Oak Ridge National Laboratory by the Scientific User Facilities Division, Office of Basic Energy Sciences, U.S. Department of Energy (J.C.I.). This research used resources of the National Energy Research Scientific Computing Center, which is supported by the Office of Science of the U.S. Department of Energy under Contract No. DE-AC02-05CH11231.

REFERENCES AND NOTES

1. Kang, B.; Ceder, G. Battery Materials for Ultrafast Charging and Discharging. *Nature* **2009**, *458*, 190–193.
2. Chiang, Y.-M. Building a Better Battery. *Science* **2010**, *330*, 1485–1486.
3. Aricò, A. S.; Bruce, P.; Scrosati, B.; Tarascon, J.-M.; Van Schalkwijk, W. Nanostructured Materials for Advanced Energy Conversion and Storage Devices. *Nat. Mater.* **2005**, *4*, 366–377.
4. Thackeray, M. M.; Kang, S.-H.; Johnson, C. S.; Vaughey, J. T.; Benedek, R.; Hackney, S. Li_2MnO_3-Stabilized $LiMO_2$ (M = Mn, Ni, Co) Electrodes for Lithium-Ion Batteries. *J. Mater. Chem.* **2007**, *17*, 3112–3125.
5. Lu, Z.; MacNeil, D.; Dahn, J. Layered Cathode Materials $Li[Ni_xLi_{(1/3-2x/3)}Mn_{(2/3-x/3)}]O_2$ for Lithium-Ion Batteries. *Electrochem. Solid-State Lett.* **2001**, *4*, A191–A194.
6. Koga, H.; Croguennec, L.; Ménétrier, M.; Mannessiez, P.; Weill, F.; Delmas, C. Different Oxygen Redox Participation for Bulk and Surface: A Possible Global Explanation for the Cycling Mechanism of $Li_{1.2}Mn_{0.54}Co_{0.13}Ni_{0.13}O_2$. *J. Power Sources* **2013**, *236*, 250–258.
7. Martha, S. K.; Nanda, J.; Veith, G. M.; Dudney, N. J. Surface Studies of High Voltage Lithium Rich Composition: $Li_{1.2}Mn_{0.52}Ni_{0.175}Co_{0.1}O_2$. *J. Power Sources* **2012**, *216*, 179–186.
8. Martha, S. K.; Nanda, J.; Veith, G. M.; Dudney, N. J. Electrochemical and Rate Performance Study of High-Voltage Lithium-Rich Composition: $Li_{1.2}Mn_{0.525}Ni_{0.175}Co_{0.1}]O_2$. *J. Power Sources* **2012**, *199*, 220–226.
9. Yang, F.; Liu, Y.; Martha, S. K.; Wu, Z.; Andrews, J. C.; Ice, G. E.; Pianetta, P.; Nanda, J. Nanoscale Morphological and Chemical Changes of High Voltage Lithium-Manganese Rich NMC Composite Cathodes with Cycling. *Nano Lett.* **2014**, *14*, 4334–4341.
10. Mohanty, D.; Kalnaus, S.; Meisner, R. A.; Rhodes, K. J.; Li, J.; Payzant, E. A.; Wood, D. L., III; Daniel, C. Structural Transformation of a Lithium-Rich $Li_{1.2}Co_{0.1}Mn_{0.55}Ni_{0.15}O_2$ Cathode during High Voltage Cycling Resolved by *In Situ* X-ray Diffraction. *J. Power Sources* **2013**, *229*, 239–248.
11. Mohanty, D.; Li, J.; Abraham, D. P.; Huq, A.; Payzant, E. A.; Wood, D. L.; Daniel, C. Unraveling the Voltage-Fade

Mechanism in High-Energy-Density Lithium-Ion Batteries: Origin of the Tetrahedral Cations for Spinel Conversion. *Chem. Mater.* **2014**, *26*, 6272–6280.
12. Armstrong, A. R.; Holzapfel, M.; Novák, P.; Johnson, C. S.; Kang, S.-H.; Thackeray, M. M.; Bruce, P. G. Demonstrating Oxygen Loss and Associated Structural Reorganization in the Lithium Battery Cathode $Li[Ni_{0.2}Li_{0.2}Mn_{0.6}]O_2$. *J. Am. Chem. Soc.* **2006**, *128*, 8694–8698.
13. Jiang, M.; Key, B.; Meng, Y. S.; Grey, C. P. Electrochemical and Structural Study of the Layered, Li-Excess Lithium-Ion Battery Electrode Material $Li[Li_{1/9}Ni_{1/3}Mn_{5/9}]O_2$. *Chem. Mater.* **2009**, *21*, 2733–2745.
14. Lin, F.; Markus, I. M.; Nordlund, D.; Weng, T.-C.; Asta, M. D.; Xin, H. L.; Doeff, M. M. Surface Reconstruction and Chemical Evolution of Stoichiometric Layered Cathode Materials for Lithium-Ion Batteries. *Nat. Commun.* **2014**, *5*, 3529.
15. Gu, M.; Belharouak, I.; Genc, A.; Wang, Z.; Wang, D.; Amine, K.; Gao, F.; Zhou, G.; Thevuthasan, S.; Baer, D. R.; Zhang, J.-G.; Browning, N. D.; Liu, J.; Wang, C. Conflicting Roles of Nickel in Controlling Cathode Performance in Lithium Ion Batteries. *Nano Lett.* **2012**, *12*, 5186–5191.
16. Lin, F.; Nordlund, D.; Weng, T.-C.; Zhu, Y.; Ban, C.; Richards, R. M.; Xin, H. L. Phase Evolution for Conversion Reaction Electrodes in Lithium-Ion Batteries. *Nat. Commun.* **2014**, *5*, 3358.
17. Lin, F.; Nordlund, D.; Markus, I. M.; Weng, T.-C.; Xin, H. L.; Doeff, M. M. Profiling the Nanoscale Gradient in Stoichiometric Layered Cathode Particles for Lithium-Ion Batteries. *Energy Environ. Sci.* **2014**, *7*, 3077–3085.
18. Lee, J.; Urban, A.; Li, X.; Su, D.; Hautier, G.; Ceder, G. Unlocking the Potential of Cation-Disordered Oxides for Rechargeable Lithium Batteries. *Science* **2014**, *343*, 519–522.
19. Van der Ven, A.; Ceder, G. Lithium Diffusion Mechanisms in Layered Intercalation Compounds. *J. Power Sources* **2001**, *97*, 529–531.
20. Xu, B.; Fell, C. R.; Chi, M.; Meng, Y. S. Identifying Surface Structural Changes in Layered Li-Excess Nickel Manganese Oxides in High Voltage Lithium Ion Batteries: A Joint Experimental and Theoretical Study. *Energy Environ. Sci.* **2011**, *4*, 2223–2233.
21. Gu, M.; Genc, A.; Belharouak, I.; Wang, D.; Amine, K.; Thevuthasan, S.; Baer, D. R.; Zhang, J.-G.; Browning, N. D.; Liu, J.; Wang, C. Nanoscale Phase Separation, Cation Ordering, and Surface Chemistry in Pristine $Li_{1.2}Ni_{0.2}Mn_{0.6}O_2$ for Li-Ion Batteries. *Chem. Mater.* **2013**, *25*, 2319–2326.
22. Boulineau, A.; Simonin, L.; Colin, J.-F.; Bourbon, C.; Patoux, S. First Evidence of Manganese−Nickel Segregation and Densification upon Cycling in Li-Rich Layered Oxides for Lithium Batteries. *Nano Lett.* **2013**, *13*, 3857–3863.
23. Liu, J.; Reeja-Jayan, B.; Manthiram, A. Conductive Surface Modification with Aluminum of High Capacity Layered $Li[Li_{0.2}Mn_{0.54}Ni_{0.13}Co_{0.13}]O_2$ Cathodes. *J. Phys. Chem. C* **2010**, *114*, 9528–9533.
24. Krivanek, O.; Corbin, G.; Dellby, N.; Elston, B.; Keyse, R.; Murfitt, M.; Own, C.; Szilagyi, Z.; Woodruff, J. An Electron Microscope for the Aberration-Corrected Era. *Ultramicroscopy* **2008**, *108*, 179–195.
25. Lin, F.; Markus, I. M.; Doeff, M. M.; Xin, H. L. Chemical and Structural Stability of Lithium-Ion Battery Electrode Materials under Electron Beam. *Sci. Rep.* **2014**, *4*, 5694.
26. Kresse, G.; Joubert, D. From Ultrasoft Pseudopotentials to the Projector Augmented-Wave Method. *Phys. Rev. B: Condens. Matter Mater. Phys.* **1999**, *59*, 1758.
27. Blöchl, P. E. Projector Augmented-Wave Method. *Phys. Rev. B: Condens. Matter Mater. Phys.* **1994**, *50*, 17953.
28. Kresse, G.; Furthmüller, J. Efficiency of *Ab-Initio* Total Energy Calculations for Metals and Semiconductors Using a Plane-Wave Basis Set. *Comput. Mater. Sci.* **1996**, *6*, 15.
29. Zhou, F.; Cococcioni, M.; Marianetti, C. A.; Morgan, D.; Ceder, G. First-Principles Prediction of Redox Potentials in Transition-Metal Compounds with LDA+ U. *Phys. Rev. B: Condens. Matter Mater. Phys.* **2004**, *70*, 235121.
30. Hautier, G.; Ong, S. P.; Jain, A.; Moore, C. J.; Ceder, G. Accuracy of Density Functional Theory in Predicting Formation Energies of Ternary Oxides from Binary Oxides and Its Implication on Phase Stability. *Phys. Rev. B: Condens. Matter Mater. Phys.* **2012**, *85*, 155208.
31. Sheppard, D.; Terrell, R.; Henkelman, G. Optimization Methods for Finding Minimum Energy Paths. *J. Chem. Phys.* **2008**, *128*, 134106.
32. Saniz, R.; Xu, Y.; Matsubara, M.; Amini, M.; Dixit, H.; Lamoen, D.; Partoens, B. A Simplified Approach to the Band Gap Correction of Defect Formation Energies: Al, Ga, and In-Doped ZnO. *J. Phys. Chem. Solids* **2013**, *74*, 45–50.